Dynamic Rupture Propagation on Fault Planes with Explicit Representation of Short Branches

Xiao Ma[1] and Ahmed Elbanna[1]

[1]Department of Civil and Environmental Engineering, University of Illinois, Urbana-Champaign, Illinois, USA

Abstract

Active fault zones are homes for a plethora of complex structural and geometric features that are expected to affect earthquake rupture nucleation, propagation, and arrest, as well as interseismic deformation. Simulation of these complexities have been largely done using continuum plasticity or scalar damage theories. In this paper, we use a highly efficient novel hybrid finite element-spectral boundary integral equation scheme to investigate the dynamics of fault zones with small scale pre-existing branches as a first step towards explicit representation of anisotropic damage features in fault zones. The hybrid computational scheme enables exact near-field truncation of the elastodynamic field allowing us to use high resolution finite element discretization in a narrow region surrounding the fault zone that encompasses the small scale branches while remaining computationally efficient. Our results suggest that the small scale branches may influence the rupture in ways that may not be realizable in homogenized continuum models. Specifically, we show that these short secondary branches significantly affect the post event stress state on the main fault leading to strong heterogeneities in both normal and shear stresses and also contribute to the enhanced generation of high frequency radiation. The secondary branches also affect off-fault plastic strain distribution and suggest that co-seismic inelasticity is sensitive to pre-existing damage features. We discuss our results in the larger context of the need for modeling earthquake ruptures with high resolution fault zone physics.

1 Introduction

The internal structure of fault zones in the upper continental crust exhibit considerable complexity. There is variation along strike in the form of bends and segmentation, and with depth due to changes in deformation mechanism including brittle to ductile transition. Mature faults consist of several basic structural elements including: (i) A zone of concentrated shear, the fault core, which is often defined by the presence of extremely comminuted gouge; (ii) A damage zone, with the primary fault core centralized in or bordering that damage zone, in addition to segmented network of several secondary cores within the damage zone. Damage zones display a greater intensity of deformation relative to the surrounding host rock, and contain features such as secondary faults and fractures, microfractures, folded strata, and comminuted grains; and (iii) host country rock with little or no damage. In general, the intensity of damage increases towards the fault core and the transition from undeformed host rock to damage zone rock often is gradual [14, 43, 3]. Overall, fault zones exhibit a combination of distributed damage as well as discrete anisotropic secondary fractures of different orientations and density [40].

Off-fault damage has been investigated extensively using numerical models that implement either off-fault plastic strain accumulation [2, 48, 18, 19] or continuum damage evolution [4, 52, 8]. The starting point in both approaches is a virgin material that has not experienced damage before. Furthermore, both approaches are found to be prone to numerical localization and have been, for the large part, constrained to scalar damage variables or isotropic formulations [20, 50]. Except for a few pioneering studies, for example [19, 45, 46], that considered off-fault dissipation generated by rough fault surfaces, most of the prior studies considered planar faults with no structural complexity. In particular, the effect of pre-existing anisotropic damage features on rupture dynamics in both the elastic and inelastic regimes, remains an area that is under studied.

An exception to the aforementioned discussion has been the investigation of the critical problem of the influence of a fault branch on the termination or continued propagation of rupture on the main fault [36], [24, 7], [10, 39, 47]. These studies suggest that the rupture may continue to propagate on the main fault without jumping to the branch, or propagate on both the main and secondary faults, or terminate on the main fault and continue on the branch. The fate of the rupture depends on the angle of the branch, the background stress field, and the rupture propagation speed. However, to the best of our knowledge, all these studies have been limited to a single long branch. Short and repeated branches that are routinely mapped in fault zones [38, 40] are largely neglected or homogenized as an effective damage variable. An outstanding challenge in explicit modeling of these anisotropic secondary features has been largely attributed to the prohibitive computational cost in terms of problem size, runtime, and memory requirements of domain based methods such as finite element or finite difference techniques.

Domain based modeling approaching are very versatile in handing complex geometries and material nonlinearities compared to boundary based methods such as the spectral boundary integral equation. However, to capture small scale details associated with short fault branches, a very fine mesh must be used to resolve the complex boundaries as well as the multiple stress concentration regions associated with the propagating rupture tips. This fine mesh is generally carried out for a significant portion of the domain to appropriately propagate the seismic waves and avoid artificial reflection from varying the mesh size over small distances. Furthermore, the simulation domain has to be truncated at some distance by imposing absorbing boundary conditions [29, 6, 5]far enough from the fault so that reflections from these boundaries do not affect the solution on the fault plane during the simulation time of interest. As a result, the computation cost of a domain-based method grows like $(L/dx)^3$ in 2D and $(L/dx)^4$ in 3D making it very challenging to incorporate small scale physics in large scale simulations.

A novel approach in addressing the above challenge has been recently presented by Klinger et al. [25] who combined optical image correlation, field observation and a new numerical method for dynamic rupture simulations using discrete finite element model to study co-seismic off fault damage generation resolving complex rupture process. Their numerical method enabled generation of co-seismic damage patterns that localize into a set of nearly periodic parallel branches. While their formulation is based on continuum damage theory, the damage parameter may numerically

localize and eventually replace by a slip weakening crack. However, what continues to be missing in this work is the effect of pre-existing secondary cracks, which is expected to influence the dynamic rupture characteristics high frequency radiation and new damage generation, in a way that is different from co-seismically generated damage in a virgin material. In this paper we plan to address this missing piece using a novel numerical scheme that enables incorporating high resolution fault zone physics and geometric structures in dynamic rupture calculations.

Here we use our recently developed hybrid computational scheme that combines a domain-based numerical method which is used to discretize a confined region encompassing the fault plane and all its related structural and material complexities, with an independent spectral boundary integral formulation that models the exterior linear elastic half spaces [22, 32]. This approach overcomes the limitations of the domain-based methods by limiting the discretization to only a subset of the whole domain but benefit from their flexibility in modeling complex geometry and material nonlinearity. The reduction in the size of the domain to be discretized enables us to use higher resolution within the fault zone to resolve the complexity of the secondary branches while saving computational cost and not compromising the accuracy of long range elastodynamic interactions which is handled exactly using the spectral boundary integrals. In this paper, we will use the hybrid scheme to investigate the dynamics of rupture propagation on fault plane with multiple short branches mimicking the fish bone architecture idealized in [36, 44].

The remainder of the paper is organized as follows. In Section 3.2, we describe the model setup and give an overview of the hybrid numerical scheme. In Section 3, we summarize the numerical simulations results from explicitly modeling the fault zone complexity. In Section 4, we discuss the new insights from the consideration of the anisotropic and discrete damage features that exist in complex fault zones. In Section 4, we summarize our conclusions.

2 Numerical method and model Setup

2.1 Hybrid Finite Element-Spectral Integral Equation Method

We solve the initial boundary value problem of dynamic fracture using the recently developed hybrid Method [32] . The hybrid method is a combination of the FEM (Finite element method) and SBI (Spectral boundary integral method), although any other domain-based method may be used in lieu of FEM. In the hybrid method, all nonlinearities, such as fault surface roughness or material nonlinearity, as well as small-scale heterogeneities, are contained in a virtual strip of a certain width that is introduced for computational purposes only (Fig. 1). Appropriate meshing techniques are then used to discretize and model this strip using FEM. The step-by-step time integration approach for the fault nodes is a central-difference explicit formulation as follows:

$$\dot{u}^{n+1/2} = \dot{u}^{n-1/2} + \Delta t\, M^{-1}(T^n - f^n) \tag{1}$$

$$u^{n+1} = u^n + \Delta t\, \dot{u}^{n+1/2} \tag{2}$$

where $\dot{}$ represents the partial derivative with respect to time and the superscript n indicates the time step index. M is the lumped mass matrix. T_n is the traction on the fault interface based on the fault discontinuity condition. The fault discontinuity condition is implemented using the Traction at Slip Nodes (TSN) method [15]. f is the internal force due to the deformation of the solid and Δt the time step.

The rest of the domain, which is homogeneous and linear-elastic, may be modeled as two half spaces coupled with this strip on each side (S^+, S^-). The elastodynamic response of these half spaces is modeled using the SBI technique. Throughout the simulation, the two methods communicate along the virtual boundaries of the strip by exchanging displacement and traction boundary conditions. The spectral formulation for this method gives an exact form of such a relationship in the Fourier domain. We use the spectral formulation introduced in [21], where the elastodynamic analysis of each half space is carried out separately. In view of the hybrid method, where SBI constitutes a boundary condition to the FEM model, we focus the description on modeling a half-space. The relationship between the traction τ_i and the resulting displacements at the boundary of a half-space may be expressed as

$$\begin{aligned}
\tau_1^{\pm}(x_1,t) &= \tau_1^{0\pm}(x_1,t) \mp \frac{\mu}{c_s}\dot{u}_1^{\pm}(x_1,t) + f_1^{\pm}(x_1,t) \\
\tau_2^{\pm}(x_1,t) &= \tau_2^{0\pm}(x_1,t) \mp \frac{(\lambda+2\mu)}{c_p}\dot{u}_2^{\pm}(x_1,t) + f_2^{\pm}(x_1,t)
\end{aligned} \tag{3}$$

where $\pm$ represents upper and lower half-plane, c_p is the pressure wave speed, c_s is the shear wave speed, τ_i^0 indicates the externally applied load (*i.e.*, at infinity); and f_i are linear functionals of the prior deformation history and are computed by the time convolution in the Fourier domain (see Appendix **??** for more details on the SBI).

The coupling of the two methods is done as follows. The FEM and SBI share nodes at the virtual boundaries introduced to truncate the FEM domain. While FEM provides SBI with the tractions along the virtual boundary, SBI returns the displacement that is to be imposed on $S^{\pm}$ of FEM. The detailed step-by-step procedure is as follows

1. Solve full time step within the FEM by solving Eq. (1 - 2) (FEM interior nodes only).
2. Set interface tractions in the SBI equal to the internal force from FEM: $\tau_i^{n,\mathrm{SBI}} = f_i^{n,\mathrm{FEM}}$, where f_i^n is given through Eq. 1.
3. Solve full time step within SBI by solving Eq. (3) for velocity and apply explicit integration scheme to get displacements.
4. Set displacements of the shared nodes in FEM equal to displacement in SBI: $u_i^{n+1,\mathrm{FEM}} = u_i^{n+1,\mathrm{SBI}}$.
5. Return to Step 1 to advance to the next time step.

A detailed illustration of the hybrid method is in Appendix A.

2.2 Model Setup

2.2.1 Material and Friction model

In this paper, we consider both linear elastic material and elasto-plastic material.

Linear elastic Material

2D plane strain elastic model is use to describe the elastic material behavior. The constitutive equation for the linear elastic material is as follows:

$$\sigma_{ij} = \lambda \delta_{ij} \varepsilon_{kk} + 2\mu \varepsilon_{ij} \tag{4}$$

where ε_{ij} is the infinitesimal strain tensor and μ, λ the Lamé parameters.

Elasto-Plastic Material

In this paper, we also consider the off-fault material to be idealized as Drucker-Prager plasticity model [17]. The Durcker-Prager model is closely related to the Mohr-Coulomb model. It descries inelastic deformation in brittle solids arising from frictional sliding of microcracks [41, 48]. We use Durcker-Prager plasticity model to mimic the inelastic effects on dynamic rupture from cracks on scales that are smaller than the scale of branches. . The yield function of the Drucker-Prager plasticity model is given by Eq.5,

$$F(\sigma_{ij}) = \sqrt{J_2} - (A + BI_1) \tag{5}$$

Here, $I_1 = \sigma_{kk}$ is the first invariant of the Cauchy stress σ_{ij} and $J_2 = \sqrt{s_{ij}s_{ij}/2}$ is the second invariant of the deviatoric stress tensor $s_{ij} = \sigma_{ij} - (\sigma_{kk}/3)\delta_{ij}$. The constants A and B are determined from experiments and are functions of the cohesion c and the angle of internal friction ϕ that are used to describe the Morh-Coulomb yield surface. When $F(\sigma_{ij}) < 0$, the material response is elastic.
Plastic flow is partitioned between various components of the plastic strain rate tensor by the flow rule. Neglecting the effect of plastic dilatancy we have:

$$\dot{\epsilon}^p_{ij} = \dot{e}^{eq}_p s_{ij}/(2\sqrt{J_2}) \tag{6}$$

Which $\dot{e}^{eq}_p = \sqrt{2\dot{e}^p_{ij}\dot{e}^p_{ij}}$ is the equivalent plastic strain rate. The equivalent plastic strain e^{eq}_p is defined trough $\dot{e}^{eq}_p = de^{eq}_p/dt$

Slip weakening friction model

In this paper, all the faults are governed by slip-weakening friction law [23]. The frictional strength is given by

$$\tau_f(D) = \begin{cases} \tau_s - (\tau_s - \tau_d)D/D_c, & D < D_c \\ \tau_d, & D \geq D_c \end{cases} \tag{7}$$

where τ_s and τ_d are the static and dynamic frictional strength and D_c the critical slip required for stress to reach the dynamic value. Continuity of displacements at the fault is enforced (*i.e.*, no slip) if the shear traction is lower than τ_f, otherwise local slip occurs. Uenishi and Rice [49] defined the characteristic length scale for frictional instability on linear slip-weakening faults. We base our reference length scale for normalizing the spatial scales in our problem on this characteristic length scale term as shown Eq.8 (omitting the constant term from [49]).

$$L_c = \frac{\mu D_c}{\tau_s - \tau_d} \tag{8}$$

Here, μ is the shear modulus, D_c is the characteristic slip distance, τ_s is the static frictional stress and τ_d is the dynamic frictional stress.

2.2.2 Geometry

We consider our fault system to exist in an infinite medium. A planar horizontal main fault is placed in the middle of the domain with secondary fault branches explicitly modeled as shown in Fig. 1. The main fault is right lateral and the secondary faults are placed on one side of the fault (on the tension side) starting at a distance L_a from the nucleation zone. This minimizes the effect of these secondary branches on the rupture nucleation. The angle between the secondary faults and main faults is assumed to be θ. While this angle may be arbitrary, here we take it to be approximately equal to the angle between the optimally oriented shear plane and the main fault using the background tectonic stress field and a Mohr-Coulomb failure criterion

$$\theta = 45^\circ + \frac{\phi}{2} - \theta_p \tag{9}$$

Eq. 9 above, ϕ is the angle of internal friction, and θ_p is the maximum principle stress direction. The secondary faults have constant spacing L_s along the fault strike. The length of each secondary fault is L_f. Vertically, the secondary fault branches are placed a small distance L_o away from the main fault. We limit the FEM discretization to a domain of length L and width W_H. The length L is taken to be $100L_c$. The width W_H is much smaller than the length L. The domain width W_H is determined by the length of secondary branches and is taken to be $4L_c$ to ensure that the FEM domain contains the complex fault geometry. All parameters are listed in Table 1.

2.2.3 Initial and Boundary Condition

We assume the domain is in static equilibrium at time $t = 0$. We consistently resolve the normal stress σ_N and tangential stress τ on all the faults from the background stress σ_{xx}, σ_{yy} and σ_{xy} using Eq. 10 .

$$\begin{aligned} \sigma_N &= \sigma_{xx} \sin^2\theta + \sigma_{yy} \cos^2\theta + 2\tau_{xy} \sin\theta \cos\theta \\ \tau &= -\sigma_{xx} \sin\theta \cos\theta + \sigma_{yy} \sin\theta \cos\theta - \tau_{xy}(\cos^2\theta - \sin^2\theta) \end{aligned} \tag{10}$$

where θ is the angle between secondary faults and the horizontal direction.We nucleate the rupture by overstressing the fault beyond the static friction strength over a localized region in its center with a width L_c.

3 Results

To normalize our results, we adopt the following dimensionless quantities for length,time, slip, slip rate and stress:

- Length, $x^* = x/L_c$
- Time, $t^* = tc_s/L_c$
- Slip, $D^* = D/D_c$
- Slip rate, $V^* = VL_c/(D_c c_s)$
- Stress, $\sigma^*_{ij} = \sigma_{ij}/(-\sigma^0_{yy})$

3.1 Elastic Domain

Fig. 2 compares several rupture metrics on the main fault plane with and without the short branches. The short branches lead to a reduction in the peak slip rate as well as the accumulated slip on the main fault plane. This may be explained by the fact that when the short branches are activated, the frictional slip on these secondary features contributes to the total energy dissipation leading to reduced slip and slip rate. The increased energy dissipation in the presence of the secondary branches also slows the rupture on the main fault and decreases the rupture propagation speed at least within the fish bone region. However, there is a slight increase in the slip near the center of the main fault (around $x^* = 0$) for the case with the short branches. The initiation and arrest of ruptures on the secondary branches lead to generation of seismic signals that are reflected back on the main fault leading to ripples in the slip rate profile that propagate backward (See Video 1 from Supplementary Material) and accumulate more slip away from the rupture tip that would not have been generated in the homogeneous medium case. The reduction in slip rate and rupture speed due to increased energy dissipation has also been previously observed in models with off-fault energy dissipation using plasticity [48] or continuum damage theories [8]. The backward propagating ripples, however, is a consequence of the geometric complexity of the model.

The secondary faults have a significant effect on the post-rupture stress distribution. Fig. 2(c) and 2(d) show that both the shear and normal stress exhibit strong spatial heterogeneities within the fish bone region after the passage of the rupture front. These strong heterogeneities are absent in the homogeneous medium case. The activation and arrest of slip on the secondary branches lead to development of normal and shear stress concentrations at their ends which load the main fault nonuniformly. These stress fluctuations lead to both stress increase as well as reduction in both of the normal and shear stress components. In particular, the normal stress is reduced to 70 % of its original value at some locations. This may suggest that some configurations of the secondary branches may even lead to fault opening although we have not observed this yet in the cases we investigated. Furthermore, the shear stress drops to 50% of its corresponding value in the homogeneous case at several points. This may also be indicative that geometric complexity may potentially lead to reversal of the shear stress sense if they cause large enough shear stress fluctuations.

Another major results in this paper is the influence of secondary branches on the high frequency generation in the bulk. Fig. 3 shows the near-field particle velocity for both cases with and without the secondary branches. For the homogeneous medium, the wave field is smooth almost everywhere with concentration of high frequencies neat the rupture tips. On the other hand, for the medium with branches, we observe coherent wave fronts that are propagating away from the tips and spaced apart periodically consistent with the periodic distribution of the secondary branches. These coherent fronts are generated due to the constructive interference of seismic radiation from the propagating rupture tip on the main fault with the seismic radiation emitted from the ruptures on the secondary branches.

To demonstrate the enhanced generation of high frequencies for the case with the fish bone structure, we plot in Fig 4. the fault parallel and fault normal components of the velocity at a station located $20L_c$ from the main fault and represented by the star in Fig. 4(c). Both components of

the velocity show high frequency fluctuations in the case of fault with branches compared to the homogeneous case. The acceleration spectra plotted in Fig. 4(c) further proves this point. The fault with small branches have a spectrum that is richer in high frequency content and furthermore shows an almost flat spectrum in the frequency range 2-20 Hz. This is consistent with observations [13, 51] and similar to the results from dynamic rupture simulation on rough faults [19]. This suggests that small scale fault branches may be a candidate for explaining near field radiation characteristics of active faults.

Another effect of the secondary faults is shown in Fig.5 which illustrates the distribution of the normal displacement of the main fault plane. For the homogeneous medium, the fault plane simply rotates. The existence of the secondary branches, however, lead to the development of undulations in the fault plane profile as shown in Fig. 5. The stress concentrations corresponding to the secondary faults, load the fault in the normal direction and promote repeated peaks in its vertical profile near the locations where the secondary branches are positioned. While the magnitude of these undulations is small, they may contribute, over several cycles, to the evolution of the main fault roughness.

3.2 Elasto-Plastic Domain

To account for additional energy dissipation mechanisms at scale smaller than the scale of the secondary branches that we haven't explicitly modeled, we consider the possibility of inelastic strain generation using an elasto-plastic material model. Since we have only considered one level of the secondary branches, the plasticity model may be used as a proxy for small scale damage that is randomly distributed and arising from microcracks or dislocation movement at nano or micro scale. Drucker-Prager plasticity is used as described in Section

Figure 6 compares several rupture metrics on the main fault plane with and without the short branches but in the presence of off-fault plasticity. In this case, the rupture may generate off-fault plastic strain if the Drucker-Pragger yield criterion is met. Consistent with the elastic case, the short branches also lead to a reduction in the peak slip rate as well as the accumulated slip on the main fault plane. The frictional slip on the secondary branches contribute to the total energy dissipation leading to reduced slip, slip rate, as well as rupture propagation speed. However, unlike in the elastic case, there is no slight increase in the slip near the center of the main fault (around $x^* = 0$) for the case with the short branches. Plasticity, which act as an additional energy sink on its own, have suppressed the backward propagating ripples and greatly reduced their effect. Overall, the slip, the slip rate, and the rupture speed are all lower in this case compared to the case of rupture propagation in elastic medium.

The effect of the secondary faults on the post-rupture stress distribution persists even with plasticity. Fig. 6(c) and 6(d) show that both the shear and normal stress exhibit strong spatial heterogeneities within the fish bone region after the passage of the rupture front. These strong heterogeneities are absent in the homogeneous medium case with off-fault plasticity. The activation and arrest of slip on the secondary branches lead to development of normal and shear stress concentrations at their ends which load the main fault nonuniformly. These stress fluctuations lead to both stress increase as well as reduction in both of the normal and shear stress components and the amplitude of the fluctuations are very similar to those generated in the elastic case indicating that they are unaffected by plasticity.

The secondary branches, as pre-existing damage features, have strong influence on the off-fault plastic strain distribution as shown in Fig. 7. While in the homogeneous case, the plastic strain distribution has the characteristic fan like shape consistent with previous studies [48, 18, 19], the plastic strain distribution is increasingly non-uniform due to the presence of the short branches. In particular, the spatial extent of the off-fault plasticity in the vicinity of the main fault is greatly reduced within the region that hosts the short branches. Furthermore, the short branches seem to have little or no plastic strain accumulation. This is probably due to their short length and limited slip rate that is not high enough to generate off-fault plasticity. However, there is a large increase in the plastic strain accumulation at the ends of the short branches due to the abrupt arrest of the slip and the associated stress concentration. Namely, there is a concentration in

plastic strain in the region between the secondary branch tip and the main fault suggesting that even if the branch is not directly connected to the main fault, this region will be severely damaged. Furthermore, there is another region of plastic strain concentration at the far end of the secondary fault. This region also does not extend along the strike of the secondary branches but is slightly bent in another direction suggesting a possible growth plane for the secondary faults if they are allowed to extend.

3.3 Rupture Characteristics with and without plasticity

Fig. 8(a) shows the rupture tip position versus time for four cases: the homogeneous medium with and without plasticity, and the fish bone structure with and without plasticity. The slope of these curves give the rupture propagation speed for each case. The existence of the secondary branches significantly reduce the rupture speed compared to the homogeneous case. The rupture propagation speed generally decreases with off-fault plastic dissipation. The rupture propagates the slowest on the main fault for the case with fish bone structure in elasto-plastic medium . An unexpected observation is that with the existence of the secondary branches, the rupture may temporally travel faster than the homogeneous case at first and then decelerate (See insert of Fig. 8(a)). This may be explained by the fact that initially the rupture speed on the main fault is small, and that when these secondary branches are activated, they generate waves that may constructively interfere with the main rupture tip, channel energy to this tip, and promote its transient acceleration. As the main rupture accelerates further, this effect is diminished and the secondary faults act primarily as energy sinks, increasing the overall energy dissipation and decelerating the main fault rupture propagation. Once the rupture tip on the main fault moves beyond the fish bone region, it accelerates further approaching the propagation speed of the rupture in the homogeneous case with and without plasticity respectively.

Fig. 8(b) show the maximum slip rate versus rupture tip position for the different cases. The secondary branches lead to a significant reduction in the peak slip rate on the main fault. Cases with off-fault plasticity also show a reduction in the peak slip rate compared to the elastic case. The existence of secondary branches also lead to high frequency oscillations in the peak slip rate as the rupture propagates indicative of enhanced radiation efficiency and high frequency generation. After the rupture on the main fault has propagated beyond the region with the fish bone architecture , the peak slip rate increases and approaches the peak slip rate values for rupture propagation in the homogeneous medium.

Fig. 9 shows the main fault frictional energy dissipation normalized by the potency at each time step versus the average slip for the fish bone case and the homogeneous case with and without plasticity. The frictional dissipation is calculated by integrating the product of the frictional stress and the slip rate over the fault length and over time $E_f = \int_0^t (\int \tau_f \dot{D} da) dt'$. The potency is defined as the integral of the slip over the fault domain $P = \int D da$. The frictional dissipation normalized by the potency gives a stress like quantity which may be taken indicative of an average frictional strength on the fault. Thus, the plots shown in Fig. 8 may be considered as modified effective slip weakening laws for the fault as a whole. The homogeneous case with and without plasticity have relatively similar effective stress-slip response. This is because the energy dissipated by off-fault plasticity is smaller than 0.1 percent of the frictional dissipation. Interestingly, the fish bone structure case with plasticity shows the least amount of frictional energy dissipation on the main fault of the four cases. This may be attributed to the other energy dissipation avenues that exist due to the combination of off-fault plasticity and frictional slip on the additional surfaces of the secondary faults. In particular, in the complex fish bone structure, the stress tends to be concentrated at the ends of the secondary faults leading to higher concentration of the plastic strain in this region. This increases the contribution to off-fault energy dissipation on the expense of the energy dissipation by frictional sliding on the main fault.

4 Discussion

Earthquake ruptures are nonlinear multiscale phenomena. The multiscale nature of the rupture process exists in both space and time. Spatially, a moderate-size earthquake typically propagates over tens of kilometres. However, the physical processes governing the rupture propagation operates within a narrow region at the rupture tip, called the process zone, which may not exceed a few millimetres in size if realistic laboratory-based friction parameters are used [33]. Between these two distant limits, multiple intermediate scales exist and need to be resolved including shear bands, branches, foliations, kinks, and spatially varying damage zones both along strike and throughout depth. Temporally, an earthquake episode, where rapid slip occurs, only lasts for few to tens of seconds. However, the time required for stress buildup and the attainment of the right condition for the initiation of the friction instability during the interseismic period may be tens to hundreds of years [26]. A fundamental challenge in earthquake source physics is to resolve this vast range of scales. In this paper we have focused on resolving the influence of one of the intermediate spatial scales, namely small scale fault branches, on the rupture dynamics of a single event. These branches are characterized as being small scale since their length is of the order of the reference length scale for nucleation in mature faults.

Our investigation of the effect of explicitly represented small scale branches on rupture dynamics reveal several results that are consistent with the more conventional method of modeling small scale damage as an effective elasto-plastic or continuum damage constitutive relations. For example, slip on these secondary faults increase the overall energy dissipation leading to a reduction in the accumulated slip, maximum slip rate, and rupture propagation speed on the main fault. However, explicit representation of these anisotropic pre-existing slip planes also lead to some novel insights that may not be captured by continuum plasticity models.

For example, the interaction of the main rupture with the short branches lead to strong heterogeneities in the final normal and shear stress distributions. These stress fluctuations may potentially lead to fault opening or reversal in the sign of the shear stress on the main fault, although, this has not been observed within the parameter range explored in this paper. Interestingly, these stress heterogeneities due to the existence of the secondary branches persist even in the presence of elasto-plastic material response. They do not get smeared or homogenized. The nonuniform stress distribution left over after the seismic event may influence the nucleation, propagation, and arrest of future seismic events. Furthermore, the secondary branches may also act as potential nucleation sites for future ruptures, that do not lie directly on the main fault, but may potentially jump over to its plane. Thus, there is significant potential that this model may form a basis for earthquake complexity.

Moreover, explicit representation of the secondary branches suggest that these features may contribute significantly to the near field high frequency generation. The constructive interference between the seismic radiation from the tip of the rupture propagating on the main fault and the ruptures propagating on the secondary faults lead to coherent high frequency generation in the bulk that is strongly correlated to the geometric distribution of the secondary branches. Furthermore, we demonstrated that the near-field acceleration spectrum in the presence of secondary faults is almost flat in the range of 2-20 Hz. This features has been widely documented in observations [51, 13]. It is also similar to what Dunham et al. [19] have observed in dynamic rupture simulations on rough faults. This suggests that complex geometric features, other than fault roughness, such as secondary short branches, may lead to similar coherent high frequency generation patterns.

During dynamic rupture propagation, energy may be dissipated on the fault plane through frictional sliding or off the fault plane in bulk processes such as damage and plasticity. Explicitly introduced secondary branches, as done here, provide additional pathways for energy dissipation through frictional sliding on these planes. Furthermore, combining secondary branches with plasticity leads to an overall increase in energy dissipation. Interestingly, however, this overall increase in energy dissipation may be accompanied by a reduction in the effective energy dissipation through frictional sliding on the fault plane as illustrated in Fig. 9. Reduced frictional dissipation corresponds to potentially lower increase in the fault temperature and thus may contribute to resolving the heat flow paradox. This is a topic of future investigation.

Different mechanisms have been proposed for fault roughness evolution [12, 3]. These mechanisms include fragmentation, wear, and healing. We have shown here that slip on secondary branches may lead to stress concentrations that load the main fault in a way that leads to undulations in the fault plane with a periodicity comparable to the spacing between the secondary branches. While the amplitude of these undulations is small, they may grow due to repeated ruptures, thus, providing an additional mechanism for fault plane roughness evolution on small scales.

In this paper, we have used linear slip weakening as the fault constitutive model. Extensive field and laboratory observations suggest that friction is a more complicated function that does not depend directly on slip but rather on the instantaneous slip rate as well as the history of the slip rate. The rate and state formulation [16, 42] has been successful in interpreting several lab and field observations. While the slip weakening friction may not be a realistic representation of the fault physics, it is a useful mathematical model. Furthermore, it may be shown that linear slip weakening friction may approximate rate and state friction response, without strong velocity weakening, with the appropriate choice of parameters. In future work, we plan to investigate our results in the framework of rate and state friction with dynamic weakening. This is crucial for extension to cycle simulations as well as in investigations of the role of large dynamic stress drops. Furthermore, it will be important to explore if time dependent post-seismic deformation may reduce the stress concentrations generated by the fish bone structure.

The recent models by Klinger et al [25] provide a pioneering step towards exploration of the influence of co-seismically evolving off-fault damage on rupture dynamics. The current paper complements these on-going efforts in the community and provides a step forward towards explicit inclusion of small scale physics in fault zone in the form of pre-existing anisotropic damage features. Continuum damage models and conventional plasticity algorithms are prone to numerical localization. In our case, we pre-define the secondary slip planes based on the background tectonic stress field. While this biases our choice for the fault plane orientations, our results are not mesh dependent. There is a need for development of computational algorithms that may nucleate and grow faults on the fly with minimum or no mesh dependency. Potential candidates include nonlocal damage and plasticity models [30, 37], extended finite element methods [27, 28], and Discontinuous Galerkin scheme with adaptive mesh refinement [34, 35, 1].

In this paper we introduced an application of the recently developed hybrid method which attests to its potential for modeling dynamic rupture with high resolution fault zone physics. While explicit representation of short branches is a start, other candidate applications are also possible. For example, we may use the hybrid method to model strain localization and shear band evolution within the gouge region [31] but while maintaining the influence of long range elastic stress transfer in the bulk. Another potential application is to model small scale damage patterns, as has been done experimentally by Biegel et al. [9] to study the transient and steady state effect of damage patterns on the rupture dynamic. These problems are too challenging for the traditional domain-based numerical schemes but the efficient domain truncation using the hybrid scheme may make them more doable.

The characteristics of the hybrid method suggests that it may also potentially be used for long-duration earthquake cycle simulations on faults with near-field material heterogeneities, material nonlinearities, or fault surface complexities. The SBI formulation offers an accurate means for truncating the wave field in both dynamic and quasi-dynamic limits, making the hybrid method capable of capturing the effects of both seismic and interseismic phases of the cycle. Moreover, by exploiting the mode truncation and adaptive time-stepping techniques already embedded in the spectral formulation by Lapusta et al. [26], it is possible to resolve the temporal multiscale nature of the rupture in an efficient manner. One can then envision coupling the SBI method with an implicit FEM scheme during the interseismic period to enable this extension. An outstanding challenge in modeling interseismic deformation on large scales is the need for efficient preconditioners for the large lineraized system of equations resulting from FEM. The hybrid method reduces the size of the domain to be discretized explicitly using the FEM and thus is expected to yield a smaller system of equations which may be solved efficiently and accurately using existing packages.

Future extensions of this work may include systematic investigation of the effect of the length, spacing and orientation of the secondary branches. The investigation may be extended to explore the influence of multiple scales and hierarchies of the secondary branches. The ultimate goal would be to use the hybrid scheme to model earthquake cycles in complex fault zone structures bridging both seismic and aseismic episodes and enabling the interplay between dynamics, stress evolution, and geometry to understand the underpinnings of earthquake complexity.

5 Conclusion

In this paper, we apply our recently developed hybrid numerical scheme to investigate the influence of explicitly represented small scale branches on rupture dynamics. This endeavor has been a challenge for most existing domain based numerical method. The complex interaction between the main fault rupture and the secondary fault branches is investigated. The results show the importance of considering near fault complexities when performing dynamic rupture simulations. The main conclusions may be summarized as follows:

- The secondary faults increases the overall energy dissipation leading to a reduction in the slip, peak slip rate and rupture propagation on the main fault.
- The activation of the secondary faults may lead to backward propagating ripples in the slip rate that increases slip far from the rupture top.
- Rupture activation, propagation, and arrest on the secondary branches lead to a strongly heterogeneous normal and shear stress fields on the main fault. These heterogeneities may potentially be large enough to cause fault opening or shear stress reversal. The complex post-event stress field would not have been generated using continuum plasticity models.
- The interaction of the seismic wave radiated from the main fault and those generated by the secondary branches promotes high frequency generation and generate high frequency fluctuations in computed seismograms.
- The secondary branches lead to evolution of normal undulations in the main fault strike.

Appendix A Hybrid Method

Independent Spectral Formulation:

The material in this section is extensively borrowed from [**?**], in which a more general treatment of the problem is provided.

$$u_1(x_1, x_2, t) = \phi_{,1}(x_1, x_2, t) + \psi_{,2}(x_1, x_2, t) \tag{A.1}$$

$$u_2(x_1, x_2, t) = \phi_{,2}(x_1, x_2, t) - \psi_{,1}(x_1, x_2, t) \tag{A.2}$$

where

$$c_p^2 \Delta\phi = \frac{\partial^2 \phi}{\partial t^2}, \quad c_s^2 \Delta\psi = \frac{\partial^2 \psi}{\partial t^2}$$

We examine one particular spectral component:

$$[\phi(x_1, x_2, t), \psi(x_1, x_2, t)] = e^{iqx_1}[\Phi(x_2, t; q), \Psi(x_2, t; q)] \tag{A.3}$$

The Laplace transform of a function f is introduced as

$$\hat{f}(p) = L[f(t)] = \int_0^\infty e^{-pt} f(t) \mathrm{d}t$$

Therefore,

$$\begin{aligned} \frac{\partial^2 \hat{\Phi}}{\partial x_2^2}(x_2, p; q) &= q^2 \alpha_p^2 \hat{\Phi}(x_2, p; q) \\ \frac{\partial^2 \hat{\Psi}}{\partial x_2^2}(x_2, p; q) &= q^2 \alpha_s^2 \hat{\Psi}(x_2, p; q) \end{aligned} \tag{A.4}$$

where

$$\alpha_p = \sqrt{1 + \frac{p^2}{q^2 c_p^2}}, \quad \alpha_s = \sqrt{1 + \frac{p^2}{q^2 c_s^2}}$$

For $x_2 > 0$

$$\hat{\Phi}(x_2, p; q) = \hat{\Phi}_0(p; q) e^{-|q|\alpha_p x_2} \tag{A.5}$$

$$\hat{\Psi}(x_2, p; q) = \hat{\Psi}_0(p; q) e^{-|q|\alpha_s x_2} \tag{A.6}$$

Substituting Eq. A.5 and Eq. A.6 in Eq. A.1 and Eq. A.2 gives

$$\begin{aligned} \hat{u}_1(x_1, x_2, t) &= e^{iqx_1} \left(iq\hat{\Phi}_0(p; q) e^{-|q|\alpha_p x_2} - |q|\alpha_s \hat{\Psi}_0(p; q) e^{-|q|\alpha_s x_2} \right) \\ \hat{u}_2(x_1, x_2, t) &= e^{iqx_1} \left(-|q|\alpha_p \hat{\Phi}_0(p; q) e^{-|q|\alpha_p x_2} - iq\hat{\Psi}_0(p; q) e^{-|q|\alpha_s x_2} \right) \end{aligned} \tag{A.7}$$

We are primarily concerned with tractions along $x_2 = 0$. Therefore,

$$u_j(x_1, x_2 = 0^+, t) = U_j(t; q) e^{iqx_1} \tag{A.8}$$

Thus,

$$\hat{U}_1(p; q) = iq\hat{\Phi}_0(p; q) - |q|\alpha_s \hat{\Psi}_0(p; q) \tag{A.9}$$

$$\hat{U}_2(p; q) = -|q|\alpha_p \hat{\Phi}_0(p; q) - iq\hat{\Psi}_0(p; q) \tag{A.10}$$

Solving for $\hat{\Phi}_0(p; q)$ and $\hat{\Psi}_0(p; q)$ yields

$$\hat{\Phi}_0(p; q) = \frac{-iq\hat{U}_1(p; q) + |q|\alpha_s \hat{U}_2(p; q)}{q^2(1 - \alpha_s \alpha_p)}, \quad \hat{\Psi}_0(p; q) = \frac{|q|\alpha_p \hat{U}_1(p; q) + iq\hat{U}_2(p; q)}{q^2(1 - \alpha_s \alpha_p)} \tag{A.11}$$

$$\begin{aligned} \hat{u}_1 = e^{i|q|x_1} \Bigg\{ & \hat{U}_1(p; q) \frac{e^{-|q|\alpha_p x_2} - \alpha_s \alpha_p e^{-|q|\alpha_s x_2}}{1 - \alpha_s \alpha_p} \\ & + \hat{U}_2(p; q) \frac{iq\alpha_s}{|q|(1 - \alpha_s \alpha_p)} (e^{-|q|\alpha_p x_2} - e^{-|q|\alpha_s x_2}) \Bigg\} \end{aligned} \tag{A.12}$$

$$\hat{u}_2 = e^{i|q|x_1}\Big\{\hat{U}_1(p;q)\frac{iq\alpha_p}{|q|(1-\alpha_s\alpha_p)}(e^{-|q|\alpha_p x_2} - e^{-|q|\alpha_s x_2}) + \hat{U}_2(p;q)\frac{e^{-|q|\alpha_s x_2} - \alpha_s\alpha_p e^{-|q|\alpha_p x_2}}{1-\alpha_s\alpha_p}\Big\} \tag{A.13}$$

Using the stress-strain relation $\sigma_{ij} = \lambda\delta_{ij}u_{k,k} + \mu(u_{i,j} + u_{j,i})$ and writing the shear stress components along the fault as $\tau_j(x_1,t) = \sigma_{2j}(x_1, x_2 = 0^+, t) = T_j(t;q)e^{iqx_1}$ yields

$$\hat{T}_1(p;q) = -\mu|q|\frac{\alpha_p(1-\alpha_s^2)}{1-\alpha_s\alpha_p}\hat{U}_1(p;q) + i\mu q\Big(2 - \frac{1-\alpha_s^2}{1-\alpha_s\alpha_p}\Big)\hat{U}_2(p;q) \tag{A.14}$$

$$\hat{T}_2(p;q) = -i\mu q\Big(2 - \frac{1-\alpha_s^2}{1-\alpha_s\alpha_p}\Big)\hat{U}_1(p;q) - \mu|q|\frac{\alpha_s(1-\alpha_s^2)}{1-\alpha_s\alpha_p}\hat{U}_2(p;q) \tag{A.15}$$

Decoupling the equations and extracting the instantaneous response gives

$$\hat{T}_1(p;q) = -\frac{\mu}{c_s}p\hat{U}_1(p;q) - \mu\Big\{|q|\frac{4\alpha_s\alpha_p - (1+\alpha_s^2)}{\alpha_s(1-\alpha_s^2)} - \frac{p}{c_s}\Big\}\hat{U}_1(p;q) \tag{A.16}$$

$$\hat{T}_2(p;q) = -\frac{(\lambda+2\mu)}{c_p}p\hat{U}_1(p;q) - \Big\{|q|\mu\frac{4\alpha_s\alpha_p - (1+\alpha_s^2)}{\alpha_p(1-\alpha_s^2)} - \frac{\lambda+2\mu}{c_s}p\Big\}\hat{U}_2(p;q) \tag{A.17}$$

for the upper half-plane. Similar expressions can be obtained for the lower half-plane. In the time domain, these relationships translate to

$$\begin{aligned}\tau_1^{\pm}(x_1,t) &= \tau_0(x_1,t) \mp \frac{\mu}{c_s}\frac{\partial u_1^{\pm}}{\partial t} + f_1^{\pm}(x_1,t),\\ \tau_2^{\pm}(x_1,t) &= \tau_0(x_1,t) \mp \frac{(\lambda+2\mu)}{c_p}\frac{\partial u_2^{\pm}}{\partial t} + f_2^{\pm}(x_1,t),\end{aligned} \tag{A.18}$$

where f is a linear functional of the prior deformation history and can be expressed in terms of its spectral components as $f_j(x_1,t) = F_j(t;q)e^{iqx_1}$. These components are given in [11] as

$$\begin{aligned}F_1^{\pm}(t;q) =& \mp\mu|q|\int_0^t H_{11}(|q|c_s t')U_1^{\pm}(t-t';q)|q|c_s\mathrm{d}t' + i(2-\eta)\mu q U_2^{\pm}(t;q)\\ &+ i\mu q\int_0^t H_{12}(|q|c_s t')U_2^{\pm}(t-t;q)|q|c_s\mathrm{d}t',\\ F_2^{\pm}(t;q) =& \mp\mu|q|\int_0^t H_{22}(|q|c_s t')U_2^{\pm}(t-t';q)|q|c_s\mathrm{d}t' - i(2-\eta)\mu q U_1^{\pm}(t;q)\\ &- i\mu q\int_0^t H_{12}(|q|c_s t')U_1^{\pm}(t-t';q)|q|c_s dt',\end{aligned} \tag{A.19}$$

where $\eta = c_p/c_s$ and H_{ij} are the convolution kernels, which are defined by the following inverse Laplace transforms

$$\begin{aligned}H_{11}(T) =& L^{-1}\left[\frac{s^2\sqrt{s^2+\eta^2}}{\sqrt{s^2+\eta^2}\sqrt{s^2+1}-\eta} - s\right],\\ H_{12}(T) =& L^{-1}\left[\frac{\eta s^2}{\eta - \sqrt{s^2+\eta^2}\sqrt{s^2+1}} + \eta\right],\\ H_{22}(T) =& L^{-1}\left[\frac{s^2\sqrt{s^2+1}}{\sqrt{1+s^2/\eta^2}\sqrt{s^2+1}-1} - \eta s\right],\end{aligned} \tag{A.20}$$

where $s = p/|q|c_s$ is the nondimensional Laplace transform variable. The kernels can be inverted numerically.

Update Scheme for the SBIE:

The time integration scheme used in the SBI is explicit and given by sampling

$$u_i^{\pm n+1} = u_i^{\pm^n} + \Delta t\dot{u}_i^{\pm n+1} \tag{A.21}$$

where the velocity is found by solving Eq. (3), which results in

$$\begin{aligned} \dot{u}_1^{\pm^{n+1}} &= \pm\frac{c_s}{\mu}(f_1^{\pm^{n+1}} + \tau_1^{0\pm} - \tau_1^{\pm^{n+1}}) \\ \dot{u}_2^{\pm^{n+1}} &= \pm\frac{c_p}{\lambda+2\mu}(f_2^{\pm^{n+1}} + \tau_2^{0\pm} - \tau_2^{\pm^{n+1}}) \end{aligned} \tag{A.22}$$

where τ_1 and τ_2 are computed from the nodal forces from the finite element method at the shared nodes

References

[1] R. Abedi, B. Petracovici, and R. Haber, *A space–time discontinuous Galerkin method for linearized elastodynamics with element-wise momentum balance*, Computer Methods in Applied Mechanics and Engineering, 195 (2006), pp. 3247–3273.

[2] D. J. Andrews, *Rupture dynamics with energy loss outside the slip zone*, Journal of Geophysical Research, 110 (2005), p. B01307.

[3] Y. Ben-Zion and C. G. Sammis, *Characterization of Fault Zones*, Pure and Applied Geophysics, 160 (2003), pp. 677–715.

[4] Y. Ben-Zion and Z. Shi, *Dynamic rupture on a material interface with spontaneous generation of plastic strain in the bulk*, Earth and Planetary Science Letters, 236 (2005), pp. 486–496.

[5] J.-P. Berenger, *A perfectly matched layer for the absorption of electromagnetic waves*, 1994.

[6] P. Bettess, *Infinite elements*, International Journal for Numerical Methods in Engineering, 11 (1977), pp. 53–64.

[7] H. S. Bhat, R. Dmowska, J. R. Rice, and N. Kame, *Dynamic slip transfer from the Denali to totschunda faults, Alaska: Testing theory for fault branching*, Bulletin of the Seismological Society of America, 94 (2004), pp. 202–213.

[8] H. S. Bhat, A. J. Rosakis, and C. G. Sammis, *A Micromechanics Based Constitutive Model for Brittle Failure at High Strain Rates*, Journal of Applied Mechanics, 79 (2012), p. 031016.

[9] R. Biegel, H. Bhat, C. Sammis, and A. Rosakis, *The effect of asymmetric damage on dynamic shear rupture propagation I: No mismatch in bulk elasticity*, Tectonophysics, 493 (2010), pp. 254–262.

[10] R. L. Biegel, C. G. Sammis, and A. J. Rosakis, *Interaction of a Dynamic Rupture on a Fault Plane with Short Frictionless Fault Branches*, Pure and Applied Geophysics, 164 (2007), pp. 1881–1904.

[11] M. S. Breitenfeld and P. H. Geubelle, *Numerical analysis of dynamic debonding under 2D in-plane and 3D loading*, International Journal of Fracture, 93 (1998), pp. 13–38.

[12] E. E. Brodsky, J. D. Kirkpatrick, and T. Candela, *Constraints from fault roughness on the scale-dependent strength of rocks*, Geology, 44 (2016), pp. 19–22.

[13] X. Chen, *Near-field ground motion from the Landers earthquake*, (1995).

[14] F. M. Chester, J. P. Evans, and R. L. Biegel, *Internal structure and weakening mechanisms of the San Andreas Fault*, Journal of Geophysical Research: Solid Earth, 98 (1993), pp. 771–786.

[15] S. M. Day, *Three-dimensional finite difference simulation of fault dynamics: Rectangular faults with fixed rupture velocity*, Bulletin of the Seismological Society of America, 72 (1982), pp. 705–727.

[16] J. H. Dieterich, *Modeling of rock friction: 1. Experimental results and constitutive equations*, Journal of Geophysical Research: Solid Earth, 84 (1979), pp. 2161–2168.

[17] D. C. Drucker and W. Prager, *Soil mechanics and plastic analysis or limit design*, Quarterly of Applied Mathematics, 10 (1952), pp. 157–165.

[18] E. M. Dunham, D. Belanger, L. Cong, and J. E. Kozdon, *Earthquake Ruptures with Strongly Rate-Weakening Friction and Off-Fault Plasticity, Part 1: Planar Faults*, Bulletin of the Seismological Society of America, 101 (2011), pp. 2296–2307.

[19] E. M. Dunham, D. Belanger, L. Cong, and J. E. Kozdon, *Earthquake ruptures with strongly rate-weakening friction and off-fault plasticity, part 2: Nonplanar faults*, Bulletin of the Seismological Society of America, 101 (2011), pp. 2308–2322.

[20] K. Duru and E. M. Dunham, *Dynamic earthquake rupture simulations on nonplanar faults embedded in 3D geometrically complex, heterogeneous elastic solids*, Journal of Computational Physics, 305 (2016), pp. 185–207.

[21] R. J. R. Geubelle, Philipppe H., *A Spectral Method for Three-Dimensional Fracture Problems*, Journal of the Mechanics and Physics of Solids, 43 (1995), pp. 1791–1824.

[22] S. Hajarolasvadi and A. E. Elbanna, *A new hybrid numerical scheme for modelling elastodynamics in unbounded media with near-source heterogeneities*, Geophysical Journal International, 211 (2017), pp. 851–864.

[23] Y. Ida, *Cohesive force across the tip of a longitudinal-shear crack and Griffith's specific surface energy*, Journal of Geophysical Research, 77 (1972), pp. 3796–3805.

[24] N. Kame, J. R. Rice, and R. Dmowska, *Effects of prestress state and rupture velocity on dynamic fault branching*, Journal of Geophysical Research: Solid Earth, 108 (2003), pp. 1–21.

[25] Y. Klinger, K. Okubo, A. Vallage, J. Champenois, A. Delorme, E. Rougier, Z. Lei, E. E. Knight, A. Munjiza, C. Satriano, S. Baize, R. Langridge, and H. S. Bhat, *Earthquake Damage Patterns Resolve Complex Rupture Processes*, Geophysical Research Letters, (2018), pp. 279–287.

[26] N. Lapusta, J. R. Rice, Y. Ben-Zion, and G. Zheng, *Elastodynamic analysis for slow tectonic loading with spontaneous rupture episodes on faults with rate- and state-dependent friction*, Journal of Geophysical Research, 105 (2000), p. 23765.

[27] F. Liu and R. I. Borja, *An extended finite element framework for slow-rate frictional faulting with bulk plasticity and variable friction*, International Journal for Numerical and Analytical Methods in Geomechanics, 33, pp. 1535–1560.

[28] ——, *Extended finite element framework for fault rupture dynamics including bulk plasticity*, International Journal for Numerical and Analytical Methods in Geomechanics, 37, pp. 3087–3111.

[29] J. Lysmer and R. L. Kuhlemeyer, *Finite dynamic model for infinite media*, journal of Engineering Mechanics Division, 95 (1969), pp. 859–878.

[30] X. Ma and A. Elbanna, *Strain localization in dry sheared granular materials: A compactivity-based approach*, Phys. Rev. E, 98 (2018), p. 22906.

[31] ——, *Strain localization in dry sheared granular materials: A compactivity-based approach*, Physical Review E, 98 (2018), p. 022906.

[32] X. Ma, S. Hajarolasvadi, G. Albertini, D. S. Kammer, and A. E. Elbanna, *A hybrid finite element-spectral boundary integral approach: Applications to dynamic rupture modeling in unbounded domains*, International Journal for Numerical and Analytical Methods in Geomechanics, (2018), pp. 1–22.

[33] H. Noda, E. M. Dunham, and J. R. Rice, *Earthquake ruptures with thermal weakening and the operation of major faults at low overall stress levels*, Journal of Geophysical Research, 114 (2009), p. B07302.

[34] C. Pelties, J. de la Puente, J.-P. Ampuero, G. B. Brietzke, and M. Käser, *Three-dimensional dynamic rupture simulation with a high-order discontinuous Galerkin method on unstructured tetrahedral meshes*, Journal of Geophysical Research: Solid Earth, 117 (2012), pp. n/a–n/a.

[35] C. Pelties, A.-A. Gabriel, and J.-P. Ampuero, *Verification of an ADER-DG method for complex dynamic rupture problems*, Geoscientific Model Development, 7 (2014), pp. 847–866.

[36] A. N. B. Poliakov, R. Dmowska, and J. R. Rice, *Dynamic shear rupture interactions with fault bends and off-axis secondary faulting*, Journal of Geophysical Research, 107 (2002), pp. ESE 6–1–ESE 6–18.

[37] S. Preuss, R. Herrendörfer, T. Gerya, J.-P. Ampuero, and Y. v. Dinther, *Seismic and aseismic fault growth lead to different fault orientations.*

[38] M. Rempe, T. Mitchell, J. Renner, S. Nippress, Y. Ben-Zion, and T. Rockwell, *Damage and seismic velocity structure of pulverized rocks near the San Andreas Fault*, Journal of Geophysical Research: Solid Earth, 118 (2013), pp. 2813–2831.

[39] C.-E. Rousseau and A. J. Rosakis, *Dynamic path selection along branched faults: Experiments involving sub-Rayleigh and supershear ruptures*, Journal of Geophysical Research, 114 (2009), p. B08303.

[40] C. D. Rowe, C. Ross, M. T. Swanson, S. Pollock, N. R. Backeberg, N. A. Barshi, C. E. Bate, S. Carruthers, S. Coulson, K. Dascher-Cousineau, N. Harrichhausen, A. F. Peña Castro, H. Nisbet, P. Rakoczy, J. Scibek, H. Smith, M. S. Tarling, A. Timofeev, and E. Young, *Geometric Complexity of Earthquake Rupture Surfaces Preserved in Pseudotachylyte Networks*, Journal of Geophysical Research: Solid Earth, 123 (2018), pp. 7998–8015.

[41] J. W. Rudnicki and J. R. Rice, *Conditions for the localization of deformation in pressure-sensitive dilatant materials*, Journal of the Mechanics and Physics of Solids, 23 (1975), pp. 371–394.

[42] A. Ruina, *Slip instability and state variable friction laws*, Journal of Geophysical Research: Solid Earth, 88 (1983), pp. 10359–10370.

[43] H. M. Savage and E. E. Brodsky, *Collateral damage: Evolution with displacement of fracture distribution and secondary fault strands in fault damage zones*, Journal of Geophysical Research: Solid Earth, 116 (2011).

[44] J. M. Seismological Society of America., J. R. Unruh, W. R. Lettis, and T. D. Rubin, *Bulletin of the Seismological Society of America.*, vol. 84, Seismological Society of America, 6 1911.

[45] Z. Shi and S. M. Day, *Rupture dynamics and ground motion from 3-D rough-fault simulations*, Journal of Geophysical Research: Solid Earth, 118 (2013), pp. 1122–1141.

[46] Y. Tal, B. H. Hager, and J. P. Ampuero, *The Effects of Fault Roughness on the Earthquake Nucleation Process*, Journal of Geophysical Research: Solid Earth, 123 (2018), pp. 437–456.

[47] E. L. Templeton, A. Baudet, H. S. Bhat, R. Dmowska, J. R. Rice, A. J. Rosakis, and C.-E. Rousseau, *Finite element simulations of dynamic shear rupture experiments and dynamic path selection along kinked and branched faults*, Journal of Geophysical Research, 114 (2009), p. B08304.

[48] E. L. Templeton and J. R. Rice, *Off-fault plasticity and earthquake rupture dynamics: 1. Dry materials or neglect of fluid pressure changes*, Journal of Geophysical Research: Solid Earth, 113 (2008), pp. 1–19.

[49] K. Uenishi and J. R. Rice, *Universal nucleation length for slip-weakening rupture instability under nonuniform fault loading*, Journal of Geophysical Research: Solid Earth, 108 (2003).

[50] C. Uphoff, S. Rettenberger, M. Bader, E. H. Madden, T. Ulrich, S. Wollherr, and A.-A. Gabriel, *Extreme scale multi-physics simulations of the tsunamigenic 2004 sumatra megathrust earthquake*, in Proceedings of the International Conference for High Performance Computing, Networking, Storage and Analysis on - SC '17, New York, New York, USA, 2017, ACM Press, pp. 1–16.

[51] D. J. Wald and T. H. Heaton, *Spatial and temporal distribution of slip for the 1992 Landers, California, earthquake*, Bulletin of the Seismological Society of America, 84 (1994), pp. 668–691.

[52] S. Xu, Y. Ben-Zion, J. P. Ampuero, and V. Lyakhovsky, *Dynamic Ruptures on a Frictional Interface with Off-Fault Brittle Damage: Feedback Mechanisms and Effects on Slip and Near-Fault Motion*, Pure and Applied Geophysics, (2015).

Tables

Medium Material Properties	**Value**
Shear Modulus μ	32 GPa
S wave velocity c_s	3.464 $km \cdot s^{-1}$
P wave velocity c_p	6.0 $km \cdot s^{-1}$
Fault constitutive Parameters	**Value**
Static friction coefficient μ_s	0.6
Dynamic friction coefficient μ_d	0.3
Characteristic slip-weakening distance d_c	0.2 m
Background Stress	**Value**
Background Vertical Stress σ_{yy}	50.0 MPa
Background Horizontal Stress σ_{xy}	10.0 MPa
Background Shear Stress σ_{xy}	20.0 MPa
Domain Geometry	**Value**
Reference length scale L_c	500 m
Length of the secondary faults L_f	$1.0L_c$
Spacing between the secondary faults L_s	$0.5L_c$
The off distance of the secondary fault from the main fault L_o	$0.1L_c$
The angle between the secondary fault and the main fault θ_n	30.0^o
Finite element cell size h	6.25m

Table 1: Parameters Description

Figures

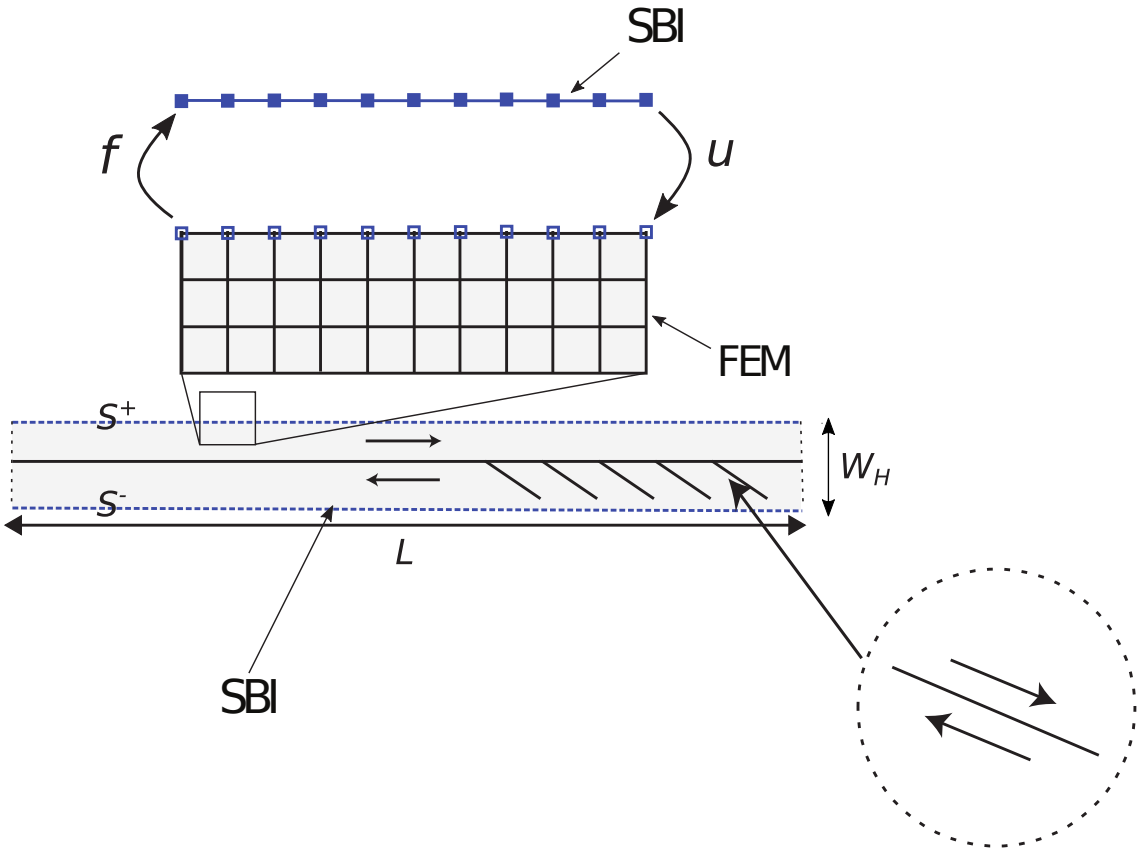

Figure 1: Schematic of the complex fault zone structure considered in this paper. The main fault lies horizontally in the middle of the domain, and the secondary branches are located in a limited region on one side of the fault (tension side). Following Poliakov et al. 2003 we call this setup a fish bone structure. All secondary faults are contained in a narrow virtual strip of dimensions L x W that is discretized using the Finite element method (FEM). On the upper and lower edges S+ and S-, the FEM is coupled with the Spectral Boundary Integral Equation which exactly model the exterior homogeneous elastic half spaces. Tractions and displacements are consistently exchanged between the two methods at the shared nodes. The details of the coupling is outlined in the text.

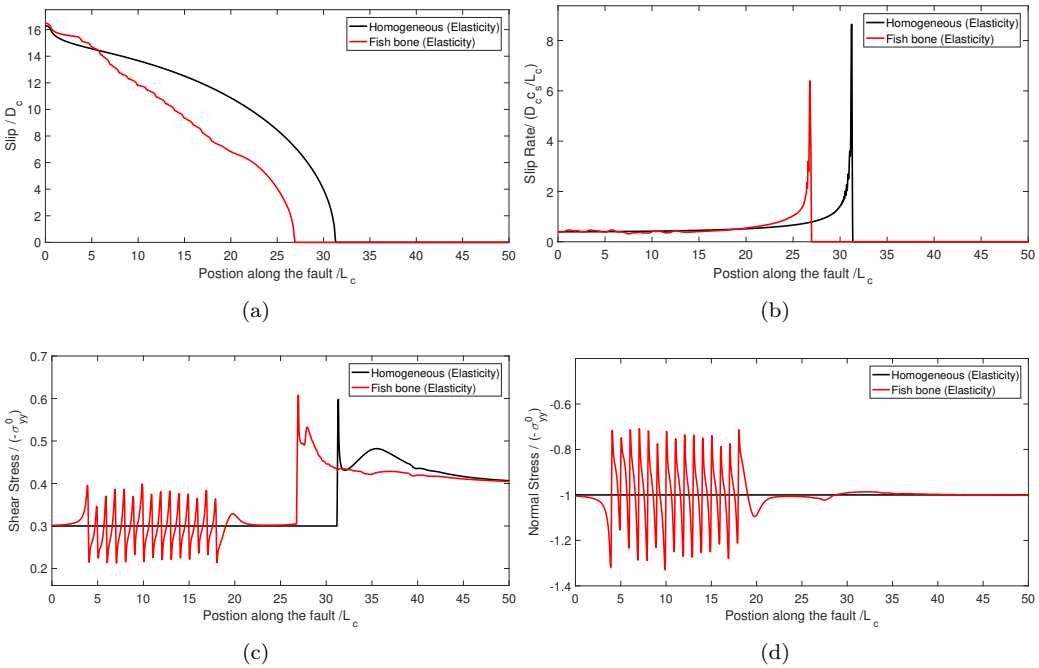

Figure 2: Slip, slip rate and shear stress distributions on the main fault, at the same point in time, with and without secondary branches for the elastic material case. (a) Slip, (b) Slip rate, (c) Shear stress distribution, and (d) Normal stress distribution. Overall, the fish bone case shows significant post-event stress heterogeneities as well as reduced slip, maximum slip rate, and rupture speed

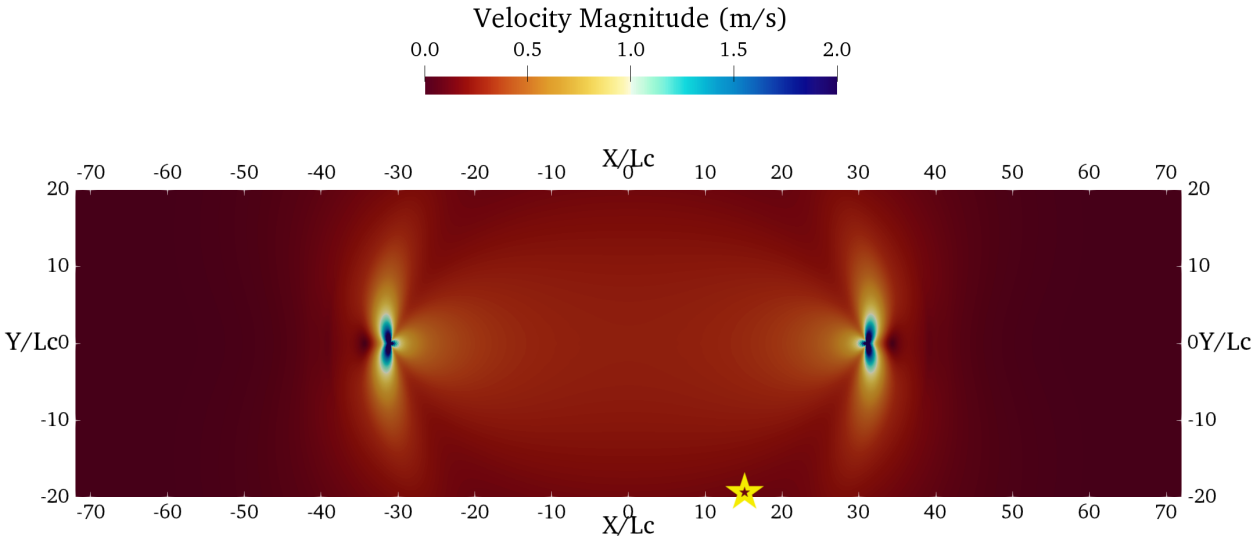

(a)

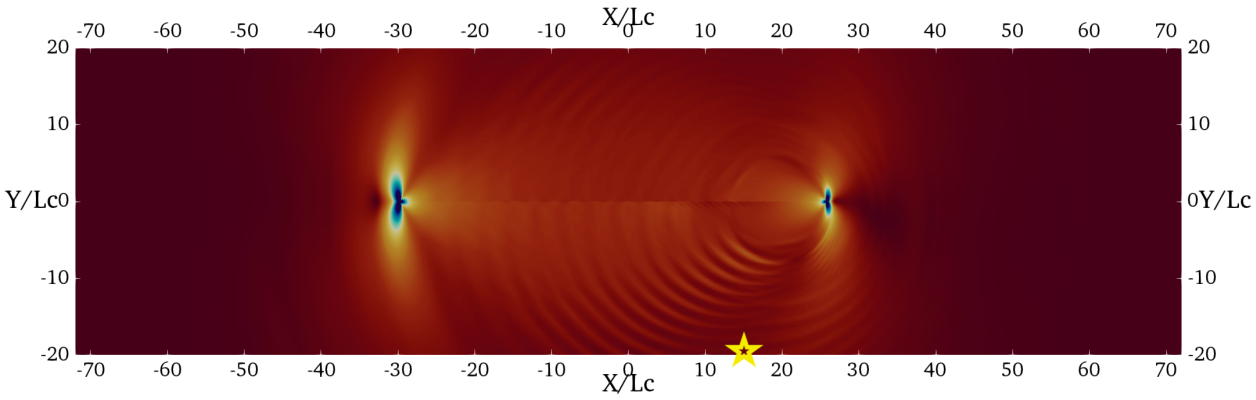

(b)

Figure 3: Contours of the bulk velocity field. (a) Homogeneous medium. (b) Domain with fish bone structure. Coherent high frequency generation emerge in the case of the fault with secondary branches (fish bone structure) and propagate away from the fault plane as concentric fringes. These high frequency waves are generated as a result of the constructive interference between the waves emitted by the main fault and the secondary branches. In the homogeneous case the high frequency wave field is localized near the rupture fronts.

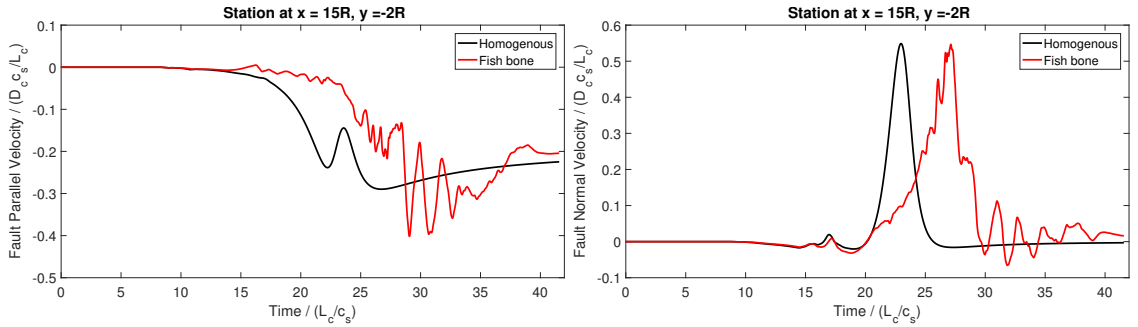

(a) (b)

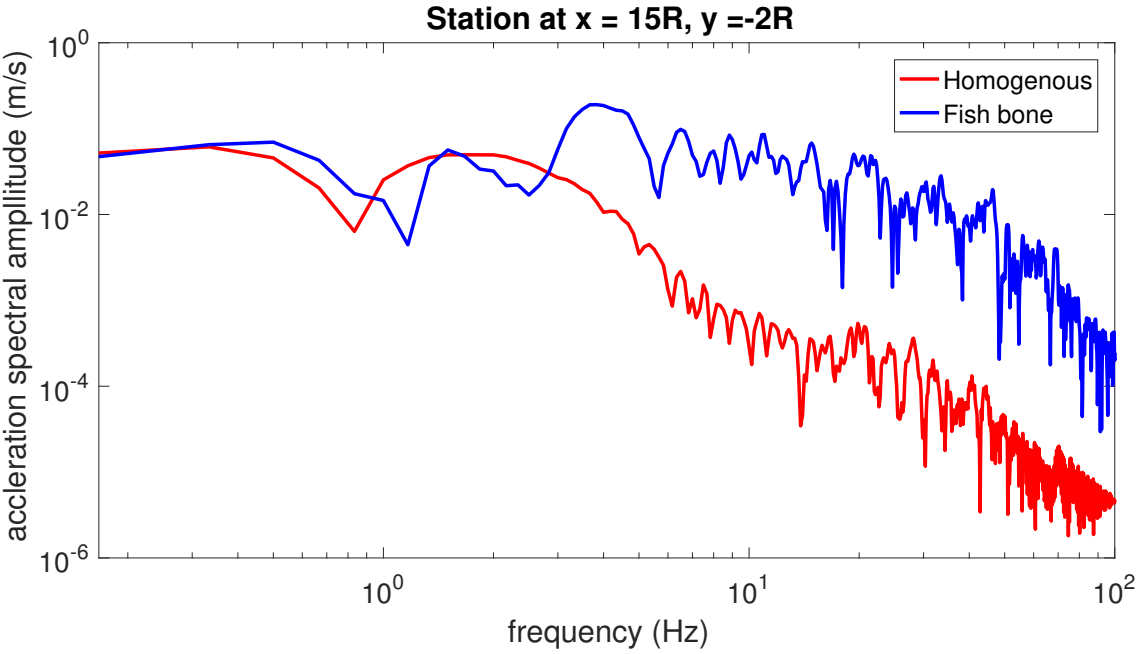

(c)

Figure 4: High frequency generation with and without secondary branches.(a),(b) Fault parallel and Fault normal velocity at station at $x* = 15R$ and $y^* = -2R$ (c) fault normal acceleration spectral amplitude at station $x* = 15R$ and $y^* = -2R$

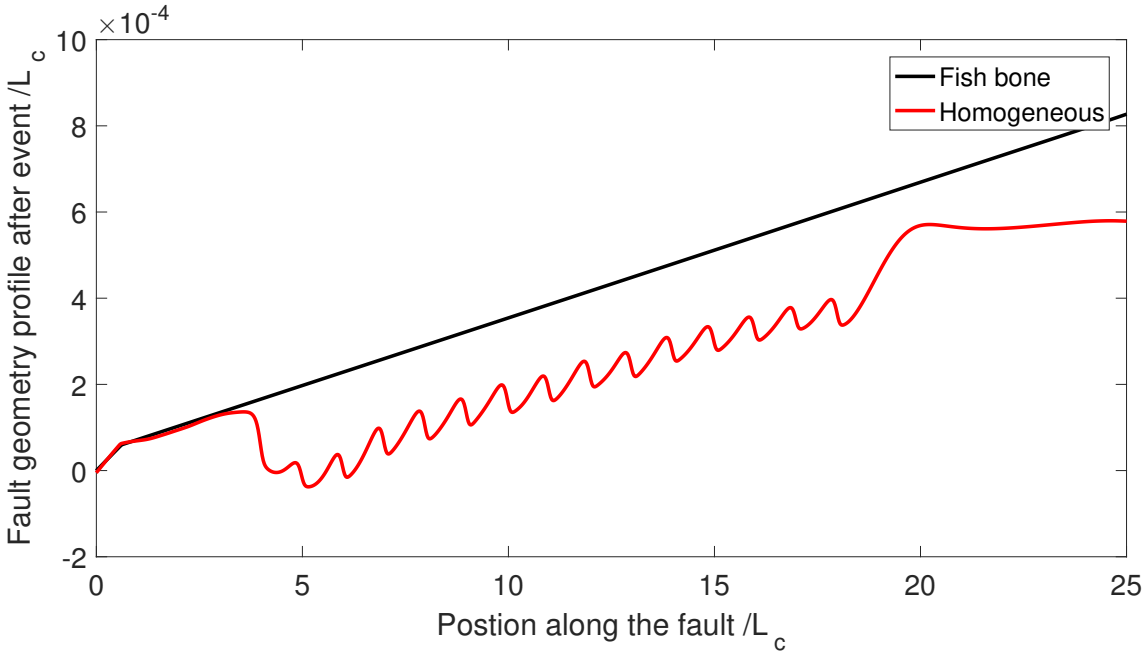

Figure 5: Normal displacement distribution with and without secondary branches. The secondary faults cause periodic undulations in the main fault profile

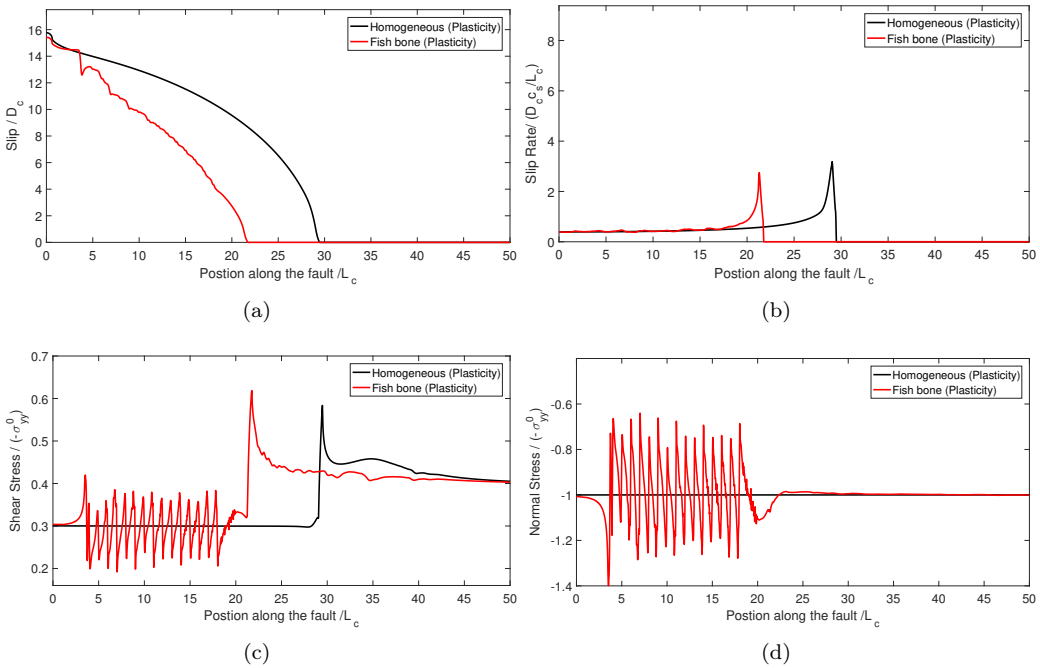

Figure 6: Slip, slip rate and shear stress distributions on the main fault, at the same point in time, with and without secondary branches for the elasto-plastic material case. (a) Slip, (b) Slip rate, (c) Shear stress distribution, and (d) Normal stress distribution. Overall, the fish bone case shows significant post-event stress heterogeneities as well as reduced slip, maximum slip rate, and rupture speed. The values of slip and maximum slip rate in the elasto-plastic case are lower than the elastic case.

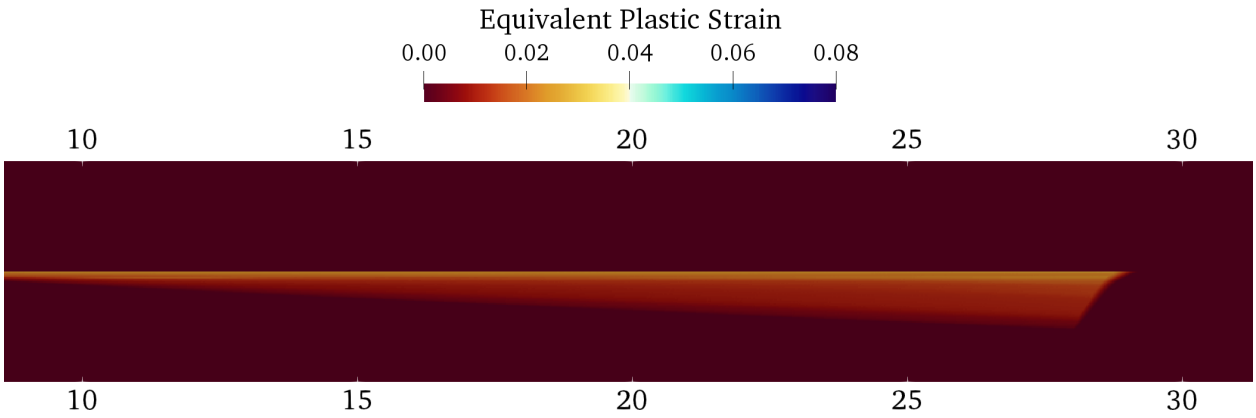

(a)

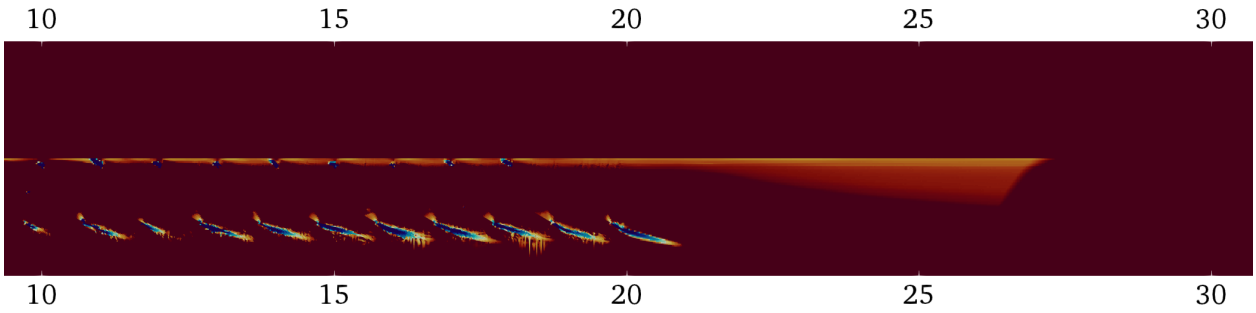

(b)

Figure 7: Equivalent Plastic Strain distribution (a) Homogeneous material (b) Fish bone structure

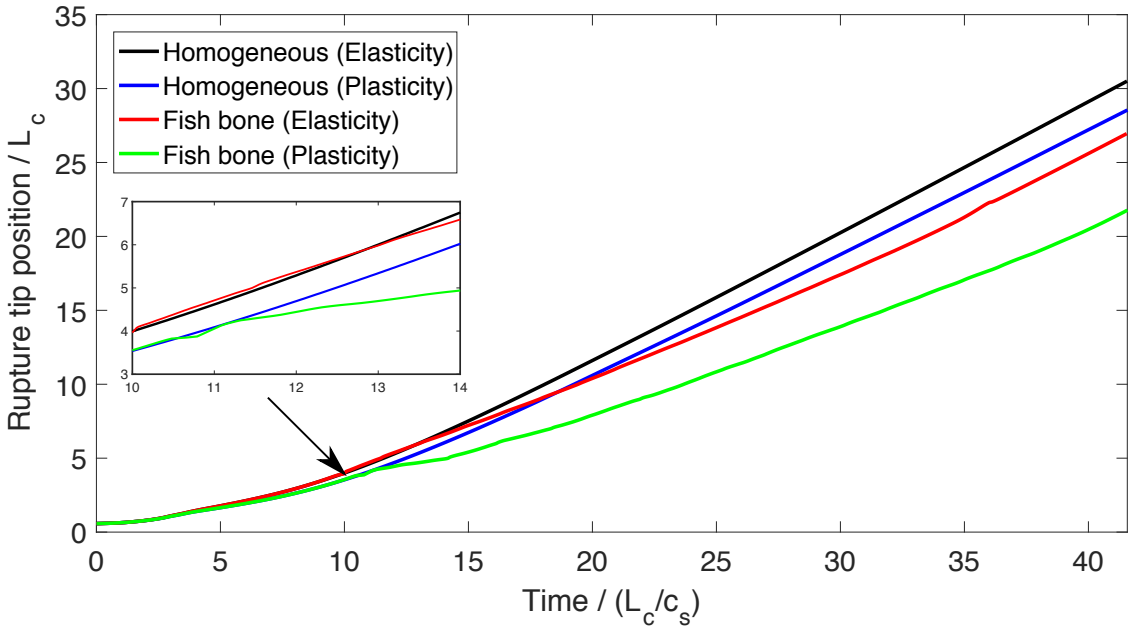

(a)

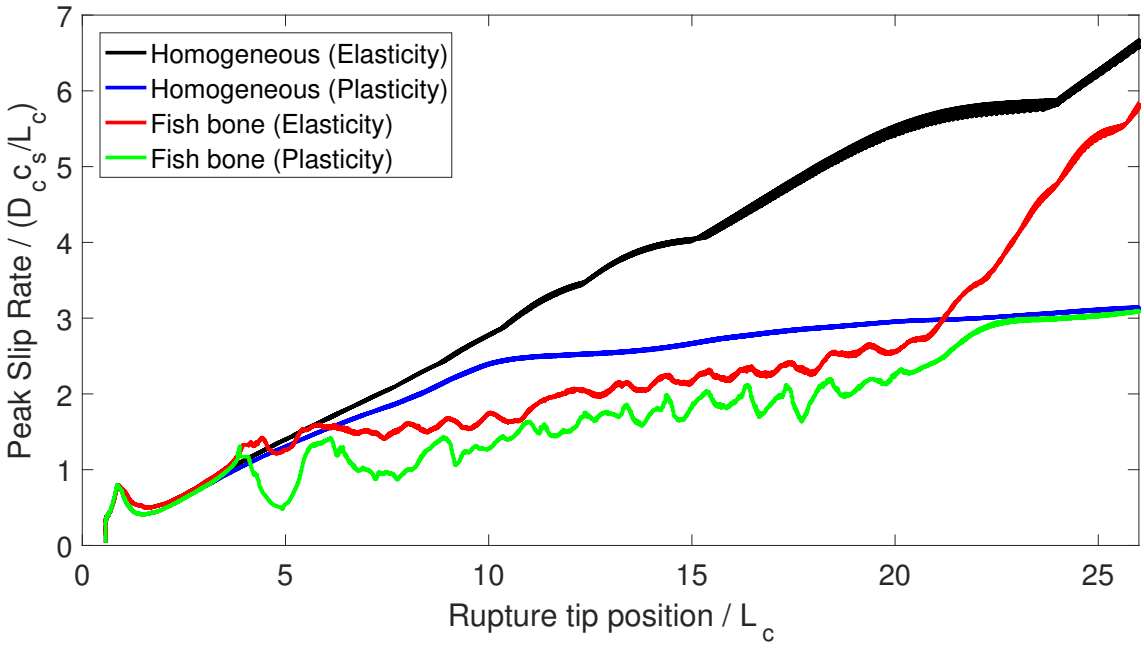

(b)

Figure 8: Comparison of rupture characteristics in the different cases (a) Rupture Tip position on the main fault as a function of time for the homogeneous and fish bone cases with elastic and elasto-plastic material models (b) Peak slip rate as a function of rupture tip position on the main fault for homogeneous and fish bone cases with elastic and elastoplastic material models

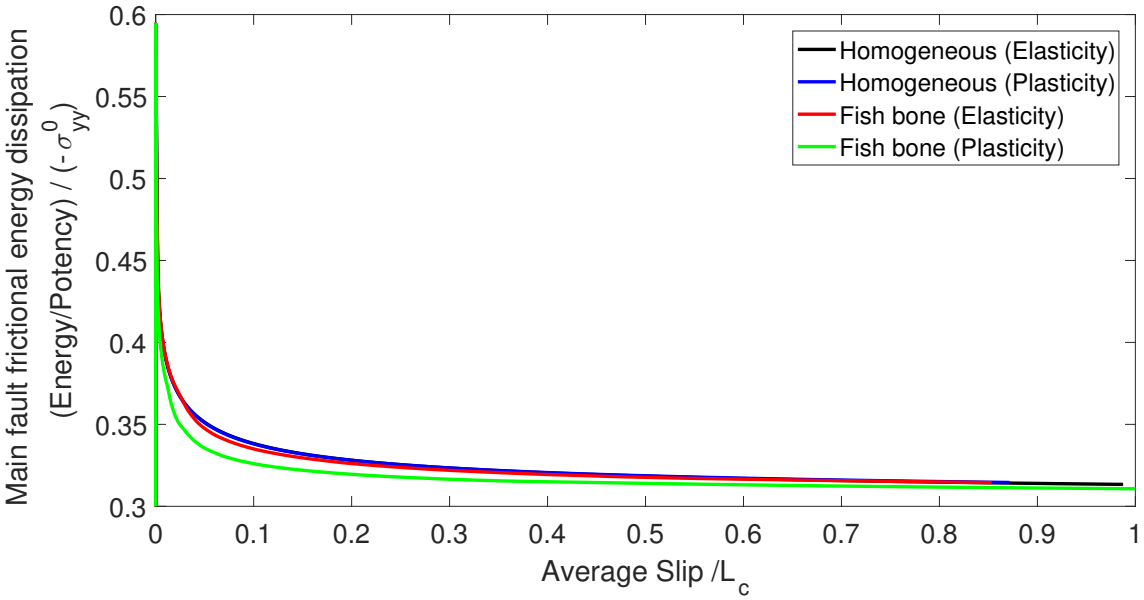

Figure 9: Frictional dissipation normalized by potency for the main fault in the four different different cases investigated in the manuscript. The homogeneous case with either elastic or elasto-plastic material models shows similar normalized frictional energy dissipation. The fish bone structure with elastic material has lower normalized frictional dissipation on the main fault than the homogeneous case due to off-fault energy dissipation by frictional sliding on the secondary branches. The fish bone structure with plasticity dissipate the least energy on the main fault as frictional heat among the four cases because more energy is being dissipated by the localized plastic deformation at the tips of the secondary faults.